3

Phase and Melting Relations of Fe_3C to 300 GPa and Carbon in the Core

Suguru Takahashi[1], Eiji Ohtani[1], Takeshi Sakai[2], Seiji Kamada[1], Shin Ozawa[1], Tatsuya Sakamaki[1], Masaaki Miyahara[1,3], Yoshinori Ito[1], Naohisa Hirao[4], and Yasuo Ohishi[4]

ABSTRACT

Carbon is a plausible candidate for a light element in the Earth's core. Here, we show that Fe_3C melts incongruently to form Fe_7C_3 and liquid at least up to 200 GPa based on in-situ X-ray diffraction measurements and textural observations of the recovered samples, and Fe_3C is stable at least up to 300 GPa at high temperatures. The C content of the liquid coexisting with Fe_7C_3 decreases and the Fe-Fe_3C eutectic composition shifts toward the Fe-rich direction with increasing pressure. The present result revealed that both Fe_3C and Fe_7C_3 are plausible constituents in the inner core.

3.1. INTRODUCTION

Seismological studies (Dziewonski & Anderson, 1981) show that the inner core is less dense than pure iron under the core conditions (Mao et al., 1990); therefore, it has been accepted that the inner core comprises iron along with lighter elements (Birch, 1964; Poirier, 1994). The density deficit of the core is estimated to be 3%–10% for the outer core (Anderson & Isaak, 2002; Shanker et al., 2004) and 2.5%–9% for the inner core (Dubrovinsky et al., 2000; Dewaele et al., 2006). Carbon is one of the major candidates for the light elements contained in the Earth's core (Hirayama et al., 1993; Wood, 1993; Dasgupta & Walker, 2008; Chi et al., 2014) because carbon has a high abundance in the solar system (Anders & Grevesse, 1989) and it can dissolve significantly in molten iron, even at ambient and upper mantle pressures (Wood, 1993; Dasgupta & Walker, 2008). Although several studies on the physical and chemical properties of iron carbides have been carried out at high pressure, there are still very limited numbers of experimental works on the phase and melting relationships in the Fe-C system to the core conditions.

Wood (1993) estimated the phase diagrams of the Fe-C system up to the pressure of the core mantle boundary (CMB) and suggested that about 2–4 wt.% of carbon could be stored in the core during the core formation stage. He suggested that the Earth's inner core is composed solely of Fe_3C. Nakajima et al. (2009) reported the phase relationships in the Fe-C system up to 30 GPa based on textural observations, chemical analysis of the recovered samples, and in-situ X-ray diffraction experiments using a Kawai-type multianvil apparatus. According to Nakajima et al. (2009), Fe_3C melts incongruently to form Fe_7C_3 and a liquid phase at 30 GPa. They proposed that Fe_7C_3 is present in the inner core. Lord et al. (2009) determined the melting temperatures of Fe_3C and Fe_7C_3 and the Fe-Fe_3C eutectic temperature up to 70 GPa from the temperature plateau obtained while increasing the laser power in a laser-heated diamond anvil cell (DAC). However, there were obvious discrepancies between the melting curves of Fe_3C and Fe_7C_3

[1] *Department of Earth and Planetary Material Sciences, Graduate School of Science, Tohoku University, Sendai, Japan*

[2] *Geodynamics Research Center, Ehime University, Matsuyama, Japan*

[3] *Department of Earth and Planetary Science, Graduate School of Science, Hiroshima University, Higashi-Hiroshima, Japan*

[4] *Japan Synchrotron Radiation Research Institute, Sayo, Japan*

Carbon in Earth's Interior, Geophysical Monograph 249, First Edition. Edited by Craig E. Manning, Jung-Fu Lin, and Wendy L. Mao.

reported by Nakajima et al. (2009) and Lord et al. (2009). In addition, Lord et al. predicted that Fe_3C decomposes to Fe and Fe_7C_3 and suggested that the inner core is composed of Fe + Fe_7C_3. On the other hand, Sata et al. (2010) reported that Fe_3C is stable up to at least 187 GPa at 300 K. In this study, high-pressure and high-temperature experiments using a double-sided laser-heated DAC were performed up to the pressure conditions of the inner core to investigate the phase and melting relationships of Fe_3C. The melting temperature of Fe_3C was determined from in-situ X-ray diffraction experiments and textural observations on recovered samples. This study aimed to reveal the phase and melting relationships of the Fe-C system under core conditions and to discuss carbon storage in the Earth's inner core.

3.2. EXPERIMENTAL PROCEDURE

We have conducted two types of experiments, in-situ X-ray diffraction experiments for determination of the phase and melting relations of Fe_3C, and a quenching experiment at 59 GPa and 2850K for textural observations of the recovered sample.

3.2.1. Sample Preparations

The starting material for the in-situ X-ray diffraction experiments was a powdered sample of cementite Fe_3C, which was synthesized from a stoichiometric mixture of iron and graphite at 3 GPa and 1273 K for 12 h using a 3000-ton Kawai-type multianvil apparatus installed at Tohoku University. The synthesized Fe_3C was confirmed to be a single phase of cementite by X-ray diffraction and SEM observations, that is, it was a single phase of cementite Fe_3C without chemical zoning and interstitial phases.

The starting material used for the quench experiment was a mixture of Fe and Fe_3C synthesized by the above procedure. The powdered mixture was laser heated using a Nd:YAG laser (λ = 1.064 μm) in an Ar atmosphere and quenched rapidly, forming a fine dendritic texture with a typical size <1 μm. The starting materials thus synthesized were analyzed based on the procedure by Dasgupta & Walker (2008) and Walker et al. (2013). After polishing the samples, the carbon content was analyzed using a wavelength-dispersive spectrometer with an EPMA (JXA-8800; JEOL, Tokyo, Japan). The calibration standard, which is cementite without zoning or interstitial phases synthesized at 3 GPa and 1273 K, was coated with aluminium. An acceleration voltage of 15 kV and a beam current of 90 nA were employed to analyze the carbon content. An LDE1H crystal in the EPMA was used to measure the carbon content in the sample. We used a defocused beam (50 μm in diameter) to perform the quantitative analysis of the bulk starting material for the quench experiment. The starting mixture for the quench experiment contained 5.2 wt.% carbon (see Table 3.1), which is slightly enriched in Fe compared to Fe_3C.

Table 3.1 The compositions of the starting material for the quenched experiment, and the quenched liquid and coexisting Fe_7C_3 recovered from 59.4 GPa and 2850 K. Numbers in parentheses are uncertainties on the last digits. The uncertainty of the composition of the quenched liquid is the compositional variation in the multiple analysis of the quenched melt region (see Figure 3.3).

		Fe (wt.%)	C (wt.%)	Total
Starting material		94.6 (3)	5.2 (4)	99.8
Recovered sample	Fe_7C_3	91.2 (1)	8.1 (1)	99.3
	Quenched liquid	93.9 (7)	4.7 (4)	98.6

3.2.2. In-Situ X-Ray Diffraction Experiments

The in-situ X-ray diffraction experiments were conducted at the BL10XU beamline at the SPring-8 facility (Hyogo, Japan) (Ohishi et al., 2008). DAC experiments were performed using a symmetric-type diamond anvil cell. Diamond anvils with various culet sizes from 40 to 350 μm were used, depending on the required experimental pressure conditions. Rhenium or tungsten gasket was pre-indented to a thickness of 10–70 μm, and a 20–120 μm diameter hole was drilled in the gasket to form a sample chamber. A foil from the powdered Fe_3C sample was prepared using a cold-compression technique. The sample foil was sandwiched between either NaCl or SiO_2 glass layers and placed in the sample chamber. The NaCl or SiO_2 layers served as a pressure-transmitting medium and as a thermal insulator.

The sample was heated using a double-sided laser heating technique employing an SPI fiber laser (λ = 1.070 μm). The shape of the fibre laser beam was adjusted to a flat-top beam using the beam-shaping system at the BL10XU beamline. This technique enabled us to decrease the temperature gradient across the sample and achieve a homogenous heating of the area with a diameter of approximately 30 μm. The temperature was determined by fitting the emission spectra from the surface of the heated sample to Planck's radiation law as a grey body formula using the typical wavelength range between 600 and 800 nm (Shen et al., 1996). The wavelength of the monochromatic X-ray beam and the distance between the sample and the X-ray detector were calibrated using X-ray diffraction patterns from CeO_2 based on the double cassette method. The typical wavelength of the X-rays was in the range of 0.4140–0.4224 Å, which was determined with

a precision of 0.04%. The X-ray beam was collimated to a diameter of 15 μm. An IP detector (RAXIS-IV; Rigaku, Tokyo, Japan) and a CCD detector (SMART APEX; Bruker AXS, Madison, WI) were used to collect the angle-dispersive X-ray diffraction data. Exposure time for the IP and CCD was 3 min and 1–10 s, respectively. The examples of the diffraction patterns are given in Figures 3.1 and 3.2. The onset of melting of the sample was determined from the disappearance of the X-ray diffraction peaks and reappearance of the peaks after quenching at high pressure, as described in previous works (Kamada et al., 2010; Campbell et al., 2007; Morard et al., 2008). Each integrated X-ray diffraction pattern, along with the 2θ angle (i.e., one dimensional X-ray diffraction profile), was analyzed using an IP analyzer and PD Indexer software package programmed by Y. Seto.

The experimental pressures were determined based on the lattice parameters of NaCl at ambient and high temperatures using the equation of state of NaCl with the B2 structure (Fei et al., 2007). An average of the lattice parameters at high temperature of the sample and those at ambient temperature at the diamond anvil surface was employed to determine the generated pressure using the procedure described by Campbell et al. (2009).

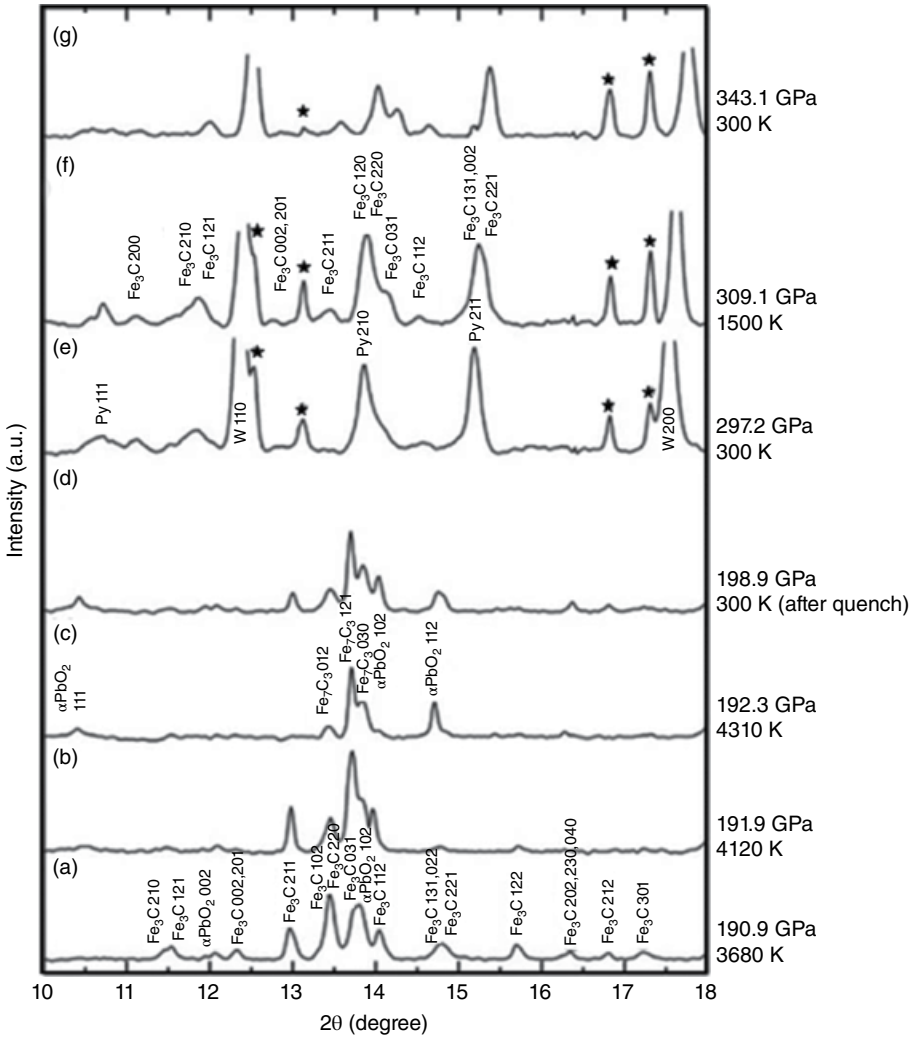

Figure 3.1 Typical examples of X-ray diffraction patterns of Fe_3C at (a)–(d) 191–199 GPa and (e)–(g) 297–343 GPa, respectively. (a) Fe_3C was a stable subsolidus phase at 190 GPa and T > 3000 K. (b) After further heating, Fe_3C peaks were observed up to 4120 K. (c) These peaks disappeared and Fe_7C_3 peaks were observed at 4310 K. (d) After quenching, the Fe_3C peaks reappeared. This result indicates that Fe_3C incongruently melted to form Fe_7C_3 and a liquid phase. (e) The Fe_3C peaks were broad before heating at 297 GPa. (f) During heating, the Fe_3C peaks became sharper at 1500 K. (g) Fe_3C was observed as a stable subsolidus phase up to 343 GPa. Key: * denotes peaks derived from outside the sample chamber since the peak positions are fixed and do not shift with pressure and temperature. See electronic version for color representation of the figures in this book.

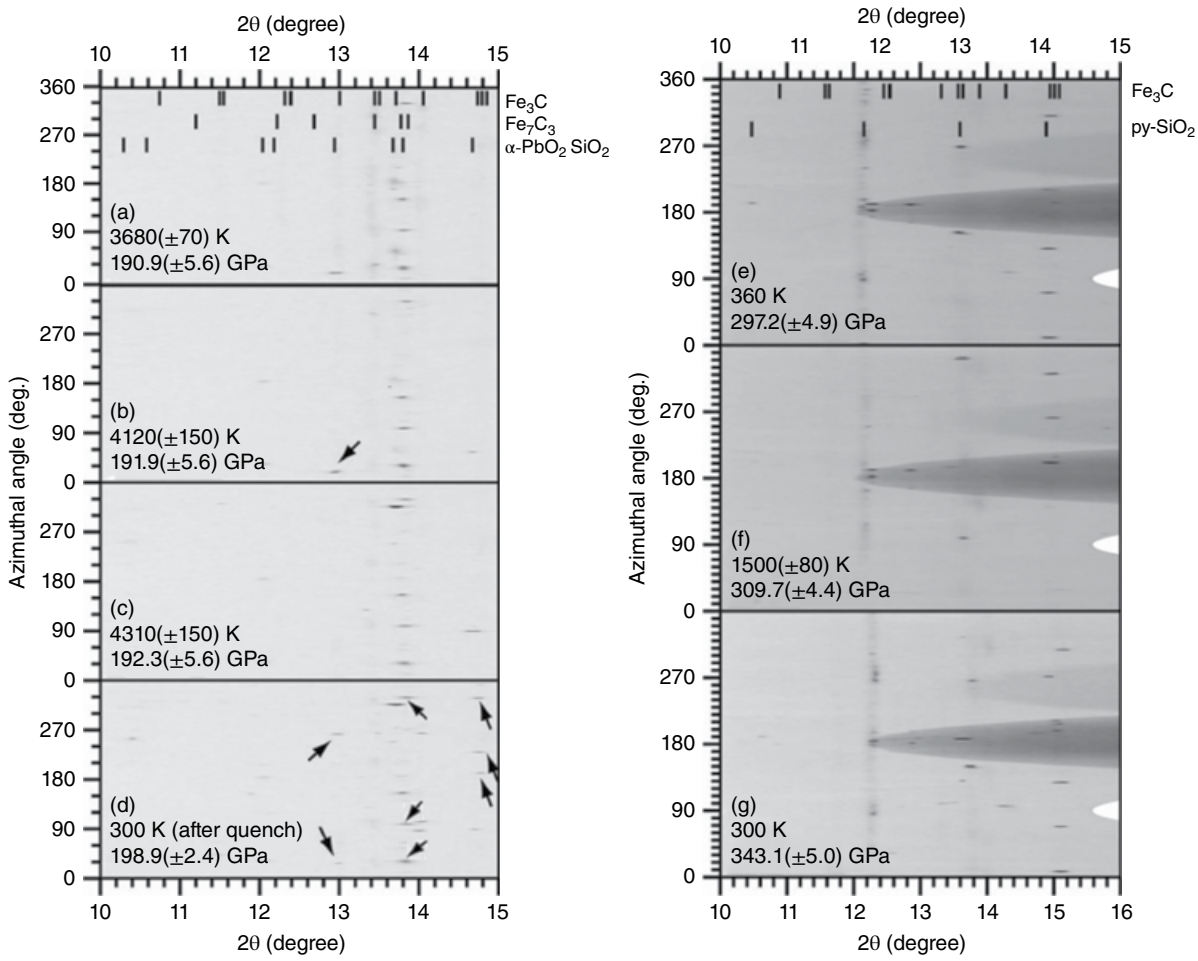

Figure 3.2 IP (a, b, c, d) and CCD (e, f, g) data obtained at high pressure and temperature. Arrows in the figures are the diffraction peaks from SiO_2 pressure medium (α-PbO_2 type SiO_2 and py, pyrite type SiO_2). These profiles correspond to one dimensional pattern shown in Figure 3.1. The peak positions of Fe_3C, Fe_7C_3, and pyrite SiO_2 are based on the equation of state of these phases by Sata et al. (2010), Chen et al. (2012), and Kuwayama et al. (2011), respectively. See electronic version for color representation of the figures in this book.

In addition, in the experiments with SiO_2 glass as the pressure-transmitting medium, pressures were estimated using the equation of state of Fe_3C (Sata et al., 2010) with thermal expansion calculated by Vočadlo et al. (2002). The results of the experiments using two different pressure media were consistent with each other as shown in Table 3.2.

3.2.3. Quench Experiment and Sample Analysis

The sample sandwiched between SiO_2 glass layers was compressed in a DAC and heated using a double-sided laser heating technique employing an SPI fiber laser (λ = 1.070 μm) with a flat top beam. The pressure was determined at room temperature using the ruby fluorescence method (Dewaele et al., 2004) and/or the pressure shift of the edge of the T_{2g} Raman band of the culet of the diamond anvil (Akahama & Kawamura, 2004). The pressure values determined by the two methods were consistent with each other. After decompression, the heated region of the recovered sample was cut by an FIB system (JEM-9320FIB; Jeol) (Miyahara et al., 2008). The texture of the prepared sample was observed using an FE-SEM (JSM-7001F; JEOL) at Tohoku University. We observed the coexistence of Fe_7C_3 and a quenched melt phase in the recovered samples. Subsequently, the chemical compositions of the coexisting phases were analyzed using the wavelength-dispersive mode of an FE-EPMA (JXA-8530F; JEOL) at Tohoku University. An accelerating voltage of 15 kV and a beam current of 30 nA were employed to analyze the carbon content, and an LDE2H crystal in the EPMA was used to measure the carbon content in the sample. We determined the calibration curve from the relationship between the carbon content

Table 3.2 Experimental conditions and observed phases.

RUN #	T (K)	P (GPa)	Observed Phases	VNaCl (Å^3)	VSiO_2 (Å^3)
In-situ X-ray diffraction experiments					
Fe3C350_061	300	68.0(9)[a]	Fe_3C, NaCl(B2)	22.78(8)	
Fe3C350_063	1360(120)	72.7(24)	Fe_3C, NaCl(B2)	22.67(2)	
Fe3C350_064	1710(200)	74.0(32)	Fe_3C, NaCl(B2)	22.66(5)	
Fe3C350_065	1770(240)	73.2(33)	Fe_3C, NaCl(B2)	22.75(12)	
Fe3C350_066	2090(70)	74.1(40)	Fe_3C, NaCl(B2)	22.76(10)	
Fe3C350_067	2270(60)	74.5(44)	Fe_3C, NaCl(B2)	22.78(10)	
Fe3C350_068	2450(70)	74.5(49)	Fe_3C, NaCl(B2)	22.83(9)	
Fe3C350_069	2630(90)	74.7(53)	Fe_3C, NaCl(B2)	22.87(9)	
Fe3C350_070	2810(80)	74.3(57)	Fe_3C, NaCl(B2)	22.96(4)	
Fe3C350_071	3020(130)	72.5(61)	Fe_7C_3 (+L), NaCl(B2)	23.18(6)	
Fe3C350_072	3310(110)	73.4(68)	Fe_7C_3 (+L), NaCl(B2)	23.18(15)	
Fe3C350_073	3420(140)	75.3(71)	NaCl(B2)	23.05(1)	
Fe3C350_074	300	68.5(5)	Fe_3C, Fe_7C_3, NaCl(B2)	22.73(4)	
Fe3C3502_030	300	47.9(16)	Fe_3C, NaCl(B2)	24.84(20)	
Fe3C3502_031	1500(50)	50.1(26)	Fe_3C, NaCl(B2)	25.04(13)	
Fe3C3502_032	1820(50)	50.7(33)	Fe_3C, NaCl(B2)	25.10(16)	
Fe3C3502_033	2010(50)	51.4(37)	Fe_3C, NaCl(B2)	25.08(12)	
Fe3C3502_034	2270(90)	51.8(43)	Fe_3C, NaCl(B2)	25.14(12)	
Fe3C3502_035	2430(110)	52.0(46)	Fe_3C, NaCl(B2)	25.17(5)	
Fe3C3502_036	2550(100)	53.1(49)	Fe_3C, NaCl(B2)	25.09(3)	
Fe3C3502_038	2790(100)	51.4(54)	Fe_7C_3 (+L), NaCl(B2)	25.41(20)	
Fe3C3502_039	3000(170)	50.4(58)	Fe_7C_3 (+L), NaCl(B2)	25.64(20)	
Fe3C3502_040	3340(150)	53.6(66)	NaCl(B2)	26.35(8)	
Fe3C3502_041	300	45.3(9)	Fe_3C, Fe_7C_3, NaCl(B2)	25.17(12)	
Fe3C130_038	300	122.0(9)	Fe_3C, NaCl(B2)	19.48(4)	
Fe3C130_039	1900(80)	138.5(39)	Fe_3C, NaCl(B2)	19.02(4)	
Fe3C130_040	2220(220)	142.2(47)	Fe_3C, NaCl(B2)	18.92(2)	
Fe3C130_041	2260(200)	142.6(48)	Fe_3C, NaCl(B2)	18.91(5)	
Fe3C130_042	2690(130)	143.5(59)	Fe_3C, NaCl(B2)	18.94(19)	
Fe3C130_043	300	134.2(32)	Fe_3C, NaCl(B2)	18.97(13)	
Fe3C130_044	2860(90)	151.3(64)	Fe_3C, NaCl(B2)	18.67(19)	
Fe3C130_045	3600(200)	153.6(83)	Fe_3C, NaCl(B2)	18.69(16)	
Fe3C130_046	3600(260)	154.5(83)	Fe_3C, NaCl(B2)	18.65(17)	
Fe3C130_047	3660(150)	152.4(84)	Fe_3C, NaCl(B2)	18.74(11)	
Fe3C130_048	3260(300)	154.7(74)	Fe_3C, NaCl(B2)	18.60(6)	
Fe3C130_049	300	144.1(27)	Fe_3C, NaCl(B2)	18.60(10)	
Fe3C130_050	300	146.3(34)	Fe_3C, NaCl(B2)	18.52(12)	
Fe3C130_051	2980(200)	149.2(67)	Fe_3C, NaCl(B2)	18.76(9)	
Fe3C130_052	3620(180)	154.7(83)	Fe_3C, NaCl(B2)	18.65(2)	
Fe3C130_055	4270(460)	157.0(100)	Fe_7C_3 (+L), NaCl(B2)	18.66(5)	
Fe3C130_056	3910(260)	153.5(90)	Fe_7C_3 (+L), NaCl(B2)	18.73(14)	
Fe3C130_057	300	142.4(22)	Fe_7C_3 (+L), NaCl(B2)	18.66(8)	
Fe3C050_002	300	183.4(22)	Fe_3C, NaCl(B2)	17.35(6)	
Fe3C050_003	1920(90)	209.1(41)	Fe_3C, NaCl(B2)	16.83(1)	
Fe3C050_004	3070(130)	217.7(73)	Fe_3C, NaCl(B2)	16.74(4)	
Fe3C050_005	2740(150)	226.1(64)	Fe_3C, NaCl(B2)	16.51(4)	
Fe3C050_008	2020(50)	214.8(44)	Fe_3C, NaCl(B2)	16.71(4)	
Fe3C050_009	2710(70)	219.6(63)	Fe_3C, NaCl(B2)	16.66(2)	
Fe3C050_012	4100(150)	229.0(101)	Fe_3C, NaCl(B2)	16.57(3)	
Fe3C050_014	3000(80)	231.5(71)	Fe_3C, NaCl(B2)	16.42(9)	
Fe3C050_015	2810(40)	228.3(66)	Fe_3C, NaCl(B2)	16.47(6)	
Fe3C050_016	300	217.4(13)	Fe_3C, NaCl(B2)	16.50(3)	
Fe3C100_010	1980(40)	187.3(56)	Fe_3C, SiO_2(α-PbO_2 type)		

(Continued)

Table 3.2 (Continued)

RUN #	T (K)	P (GPa)	Observed Phases	VNaCl (Å^3)	VSiO$_2$ (Å^3)
Fe3C100_011	2860(70)	189.2(56)	Fe_3C, SiO_2(α-PbO_2 type)		
Fe3C100_012	3680(70)	190.9(56)	Fe_3C, SiO_2(α-PbO_2 type)		
Fe3C100_013	4120(150)	191.9(56)	Fe_3C, SiO_2(α-PbO_2 type)		
Fe3C100_015	4310(150)	192.3(56)	Fe_7C_3 (+L), SiO_2(α-PbO_2 type)		
Fe3C100_016	300	198.9(24)	Fe_3C, Fe_7C_3, SiO_2(α-PbO_2 type)		
Fe3C040_018	300	297.2(49)	Fe_3C, SiO_2(pyrite type)		59.49(4)
Fe3C040_020	300	309.7(30)	Fe_3C, SiO_2(pyrite type)		58.72(19)
Fe3C040_022	1500(80)	309.7(44)	Fe_3C, SiO_2(pyrite type)		59.17(44)
Fe3C040_023	300	306.8(57)	Fe_3C, SiO_2(pyrite type)		58.81(18)
Fe3C040_025	300	313.1(31)	Fe_3C, SiO_2(pyrite type)		58.44(14)
Fe3C040_027	300	319.8(34)	Fe_3C, SiO_2(pyrite type)		58.50(13)
Fe3C040_029	1580(100)	325.8(23)	Fe_3C, SiO_2(pyrite type)		58.37(19)
Fe3C040_030	300	327.4(61)	Fe_3C, SiO_2(pyrite type)		58.18(15)
Fe3C040_032	300	321.6(83)	Fe_3C, SiO_2(pyrite type)		58.14(6)
Fe3C040_033	300	328.1(23)	Fe_3C, SiO_2(pyrite type)		57.94(10)
Fe3C040_034	300	324.8(31)	Fe_3C, SiO_2(pyrite type)		58.27(2)
Fe3C040_035	300	322.4(28)	Fe_3C, SiO_2(pyrite type)		58.16(13)
Fe3C040_038	300	322.8(27)	Fe_3C, SiO_2(pyrite type)		58.03(24)
Fe3C040_040	300	324.2(101)	Fe_3C, SiO_2(pyrite type)		58.18(44)
Fe3C040_042	300	333.6(69)	Fe_3C, SiO_2(pyrite type)		57.67(10)
Fe3C040_043	300	343.1(50)	Fe_3C, SiO_2(pyrite type)		57.30(37)
Quenched experiment					
Fe3C350lab_001	2850(200)	59.4(60)[b]	Fe_3C, Fe_7C_3, Quenched L, SiO_2		

Numbers in parentheses are uncertainties on the last digits.
[a] The pressures were determined by the equations of state B2 (Fei et al., 2007) for the runs using the NaCl pressure medium, and the equation of state of Fe_3C (Sata et al., 2010) with the thermal expansion (Vočadlo et al., 2002) for the runs with the SiO_2 glass pressure medium.
[b] The pressure was determined by the pressure dependency of the edge of T_{2g} Raman band of the diamond anvil (Akahama & Kawamura, 2004) and ruby fluorescence (Dewaele et al., 2004).

and the C Kα count rates in the standards employed (Fe and Fe_3C). The standard of Fe_3C was synthesized at 3 GPa and 1273 K. Fe_3C synthesized at this condition contains no compositional zoning nor impurities and is thus close to stoichiometry, according to Walker et al. (2013). An image of the recovered sample is shown in Figure 3.3 and the results of chemical analyses are summarized in Table 3.1.

3.3. RESULTS

3.3.1. In-Situ X-Ray Diffraction Experiments

The experiments were carried out in the pressure range 50–340 GPa and the temperature range 300–4300 K. The diffraction patterns of Fe_3C at pressures around 200 GPa and >300 GPa are shown in Figures 3.1 and 3.2. We observed Fe_3C up to 191.9 GPa and 4120 K. After heating to higher temperatures, the X-ray diffraction peaks of Fe_3C disappeared, and diffraction peaks assignable to Fe_7C_3 were observed at 192.3 GPa and 4310 K. After quenching, the diffraction peaks of Fe_3C reappeared. This indicates clearly incongruent melting of Fe_3C to Fe_7C_3 and liquid, as was reported in previous studies at low pressure around 7~14 GPa (Nakajima et al., 2009; Litasov et al., 2013; Walker et al., 2013). At higher pressure conditions, we observed X-ray diffraction peaks ascribable to Fe_3C up to 325 GPa at 1500 K and up to 343.1 GPa at 300 K (Figure 3.2). These results are consistent with preliminary data on the Fe_3C stability at 360 GPa and temperatures up to 5500 K (Tateno et al., 2010), in which a carbide was formed by reaction of Fe with diamond anvils. Although Liu et al. (2016) reported that Fe_3C decomposes to Fe and Fe_7C_3 at pressures above 160 GPa, we clearly observed the existence of Fe_3C up to 325 GPa and high temperature without decomposition, as shown in Figures 3.1 and 3.2. Chen et al. (2018) reported the sound velocities of Fe_3C up to core pressures. Our results together with previous experiments (Gao et al., 2011; Chen et al., 2014; Chen et al., 2018) indicate that Fe_3C with the cementite structure is likely to be stable in the inner core pressure and temperature conditions, although we need further detailed studies to confirm it. The experimental conditions and results are given in Table 3.2.

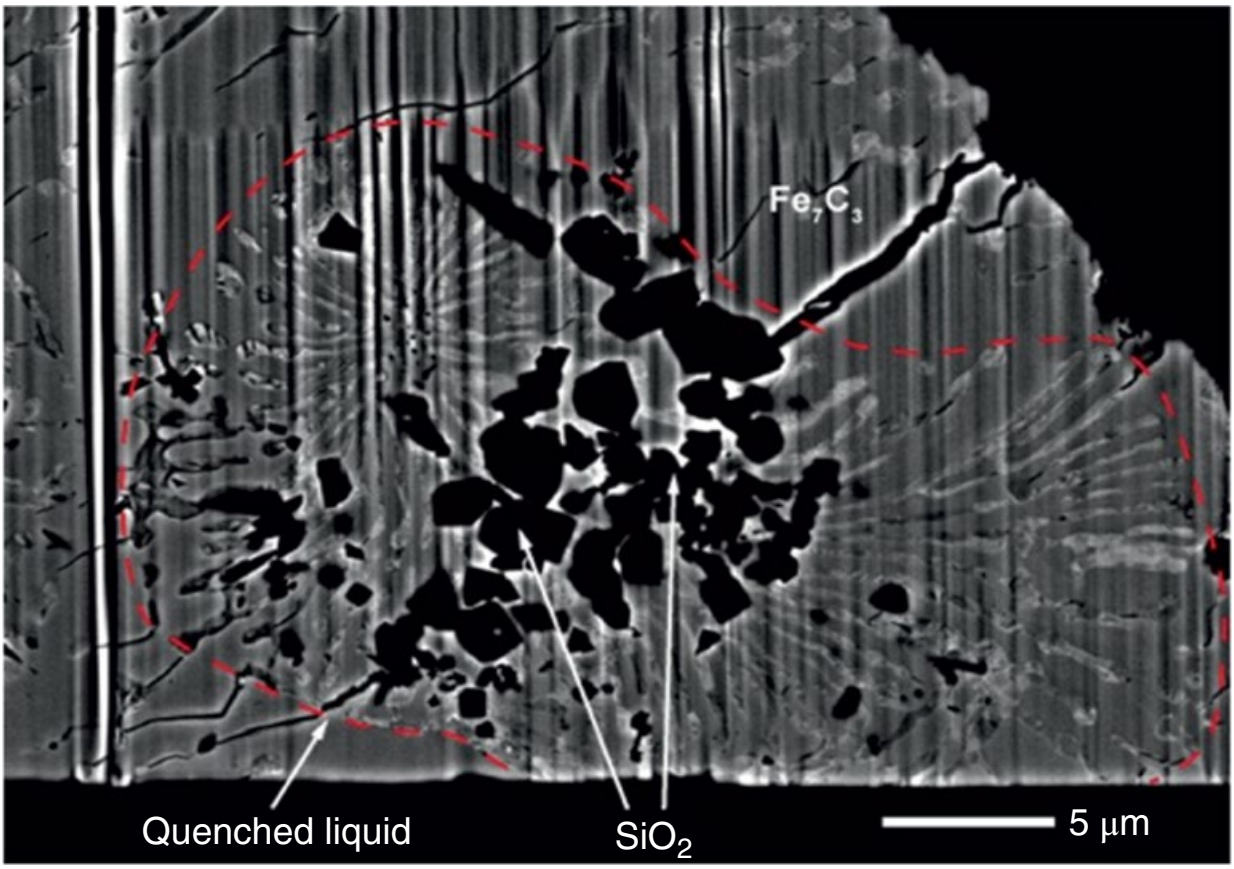

Figure 3.3 A backscattered electron microscope image of a sample recovered from 59.4 GPa and 2850 K. The area enclosed by the red dashed line shows a quenched liquid phase. SiO_2 was used as the pressure-transmitting medium. The quenched liquid is surrounded by Fe_7C_3 grains. The region outside Fe_7C_3 grains is composed of Fe_7C_3 (dark) and Fe_3C (bright) grains with granular textures. The compositions of the quenched liquid and Fe_7C_3 are given in Table 3.2. This image indicates incongruent melting of Fe_3C. See electronic version for color representation of the figures in this book.

3.3.2. Textual Observations and Chemical Analysis of the Recovered Sample

We performed textural observations of a recovered sample quenched from 59.4 GPa and 2850 K for a starting material with a bulk carbon content of 5.2 wt.%, which is slightly more enriched in Fe than the stoichiometric Fe_3C, as shown in Table 3.1. The quench texture of this run is shown in Figure 3.3. The carbon content in the quenched liquid phase was measured to be 4.7 wt.%, lower than the carbon content of the starting material. In addition, we observed Fe_7C_3 as a liquidus phase. This result confirms incongruent melting of Fe_3C to Fe_7C_3 and liquid at 59.4 GPa.

3.4. DISCUSSION

The experimental results are summarized in Figure 3.4. Our results of incongruent melting temperature of Fe_3C were fitted using Simon's equation as follows (Simon & Glatzel, 1929):

$$T_m = T_m^R \times \left(\frac{P - P^R}{A} + 1 \right)^{\frac{1}{C}}$$

where T_m and T_m^R are the melting temperature at an experimental pressure (P) and a reference pressure (P^R), respectively, and A and C are fitting parameters. This equation is employed for convenience of melting curve fitting following previous authors (Lord et al., 2009; Terasaki et al., 2011). The melting curve was fitted with the reference, P^R= 0 GPa and T_m^R = 1500 K GPa, which is the metastable incongruent melting temperature of Fe_3C at 1 bar (Benz & Elliott, 1961). The fitting parameters obtained here are A = 18.9 ± 3.3 and C = 2.4 ± 0.2. The incongruent melting temperature of Fe_3C was estimated to be 5130 ± 180 K at 330 GPa by extrapolation to the ICB pressure as shown in Figure 3.4. The fitted curve is consistent with the core isentropes and temperature at ICB estimated based on melting of mantle materials and

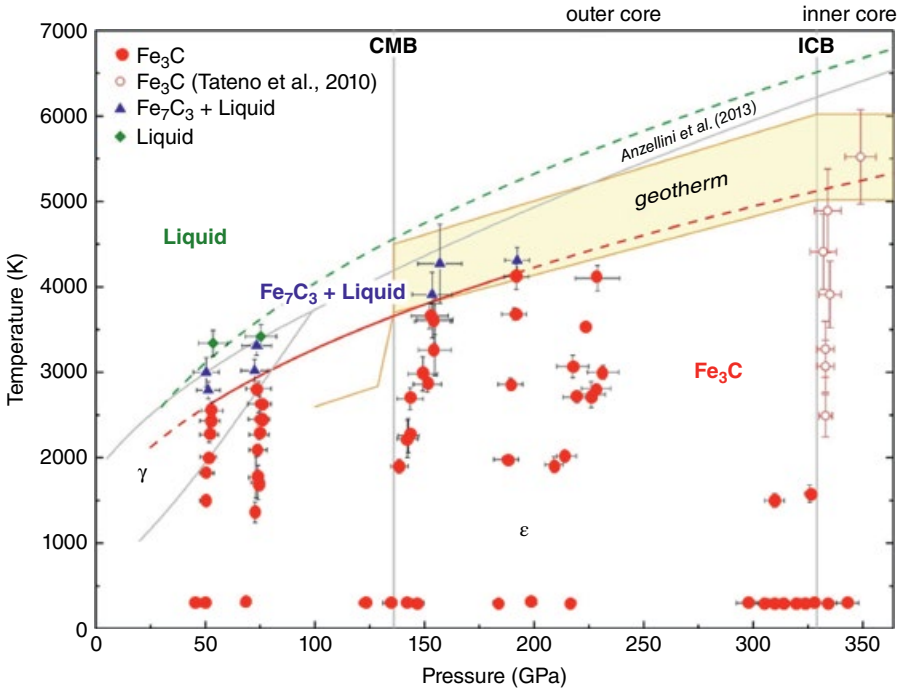

Figure 3.4 Phase diagram of Fe_3C. The solid circles, triangles, and diamonds represent Fe_3C, Fe_7C_3 + liquid, and liquid, respectively. The open circles show Fe_3C as products of the reaction between iron and the diamond anvil, as observed by Tateno et al. (2010). The grey lines show the melting and phase boundary of Fe (Anzellini et al., 2013). The solid curve is the solidus temperature fitted using Simon's equation (Simon & Glatzel, 1929). The curve represents the approximate boundaries between Fe_3C and Fe_7C_3 + liquid. The curve was fitted with the reference P^R = 0 GPa and T_m^R = 1500 K GPa (Benz & Elliott, 1961), and parameters A = 18.9 ± 3.3 and C = 2.4 ± 0.2. The liquidus curve is shown as a dashed curve, which is expressed by the parameters A = 18.9 and C= 2.4, which are assumed to be the same as the parameters of the solidus curve, and T_m^R = 1798 K and P^R= 7.7 GPa (Terasaki et al., 2014). The solidus temperature at the ICB is estimated to be 5130 K. The shaded area represents the temperature distribution of the core (Nimmo, 2015). See electronic version for color representation of the figures in this book.

energetics of the core, that is, heat flux from the core (Nimmo, 2015).

Figure 3.5 shows the phase and melting relationships of the Fe-C system from 14 GPa (Nakajima et al., 2009) to 200 GPa. The composition of the liquid formed by incongruent melting of Fe_3C at 60 GPa determined in this work (Table 3.1) is Fe-rich in composition compared to that at 14 GPa. The compositions of the peritectic liquids coexisting with Fe_7C_3 shift toward the Fe-rich side at pressures from 14 GPa to 60 GPa. This result indicates that the Fe-Fe_3C eutectic composition will also change to Fe-rich in composition, as has been shown in previous studies (Lord et al., 2009; Fei & Brosh, 2014) expanding compositional fields of liquidus Fe_3C and Fe_7C_3.

Lord et al. (2009) proposed that both hcp-Fe and Fe_7C_3 are stable as subsolidus phases and are candidates for the inner core. However, our results clearly reveal that Fe_3C is a stable carbon-bearing compound, although it melts incongruently into Fe_7C_3 and liquid at temperatures above 5130 ± 180 at 330 GPa (Figure 3.4). Therefore, both Fe_3C and Fe_7C_3 are potential stable carbon-bearing phases in the inner core.

Several authors have estimated the carbon content in the core. Wood (1993) estimated the concentration of carbon in the core to be 2–4 wt.% based on high solubility of carbon in liquid Fe and high abundance of carbon in C1 chondritic meteorites. McDonough (2003) estimated a carbon content of 0.2 wt.% from his estimation of bulk Earth composition and mass balance calculations between the mantle and core. Fiquet et al. (2009) estimated the carbon content in the core to be about 1 wt.% based on the sound velocity of Fe_3C and the preliminary reference Earth model (PREM) inner core. Mookherjee et al. (2011) estimated the maximum carbon content in the inner core to be 1.5 wt.% based on sound velocity measurements and ab initio calculations on Fe_7C_3. According to recent experiments at 1–3 GPa and 1773–2073 K, the partition coefficient of carbon between metal and silicate melts varies between 500 and 5400, which is different from previous estimations and

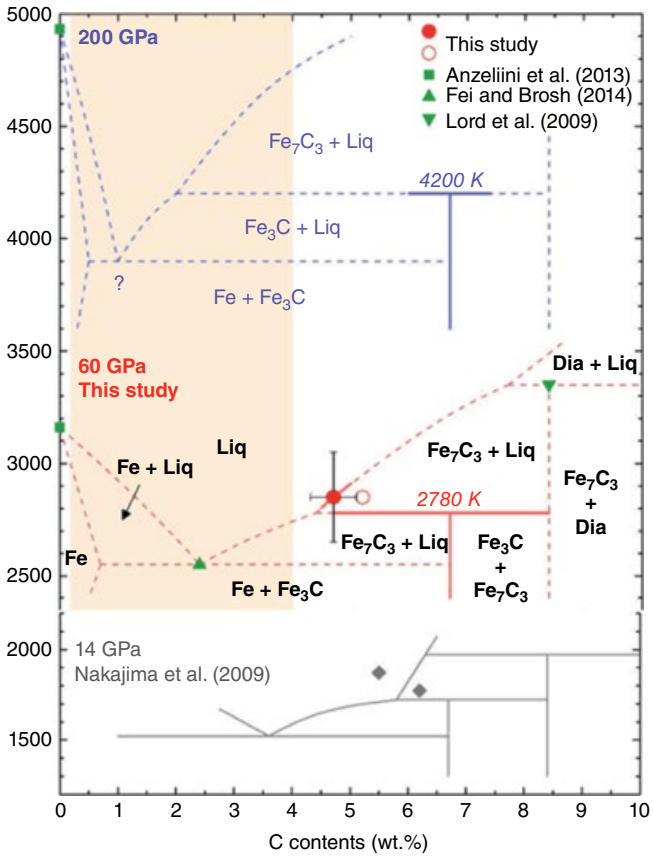

Figure 3.5 The Fe-rich portion of the Fe-C phase diagram up to 200 GPa inferred from our experiments in comparison with experiments and thermodynamic calculations at 14 GPa (Nakajima et al., 2009). The solid and open circles represent the carbon content of the quenched melt coexisting with Fe_7C_3 and the composition of the starting material in the quenching experiment at 60 GPa, respectively. The grey diamond symbols show the melt compositions at 14 GPa (Nakajima et al., 2009). The melting temperatures of Fe, solid squares, were based on the data from Anzellini et al. (2013). The eutectic composition at 60 GPa, a solid triangle, was estimated to have about 2.4 wt.% C based on the pressure shift of the Fe-Fe_3C eutectic composition by Fei and Brosh (2014). The peritectic temperature was estimated by the Simon's equation fitting of the experimental data (Figure 3.2). The shaded area represents the possible bulk carbon content in the Earth's core (Wood, 1993; McDonough, 2003; Fiquet et al., 2009). Compared to the Fe-C phase diagram at 14–60 GPa, the composition of the quenched melt coexisting with Fe_7C_3 is likely to be shifted toward the Fe-rich side with increasing pressure (Nakajima et al., 2009; Fei & Brosh, 2014). See electronic version for color representation of the figures in this book.

indicates strong partitioning to the metal, comparable with partitioning of highly siderophile elements (Chi et al., 2014). If the Earth was accreted from C1 chondrite parental bodies with high carbon content, up to 4 wt.% of carbon can be easily concentrated in the Earth's core. Therefore, the carbon content in the Earth's core is likely to be in the range 0.2–4 wt.%. The equation of state of Fe_7C_3 showed that the density of the inner core can well be explained by a single phase of Fe_7C_3 (Nakajima et al., 2011) or a mixture of 90-60 vol.% of Fe_7C_3 and 10-40% of hcp-Fe (Chen et al., 2012). The equation of state of Fe_3C determined previously (Sata et al., 2010; Litasov et al., 2013) indicates similar compression behaviors of Fe_3C to Fe_7C_3. Thus, the inner core can be explained by Fe_7C_3 or Fe_3C within the experimental uncertainty of the equation of state, assuming the ICB temperature ~5000 K. Finally, sound velocity measurements of Fe_7C_3 (Chen et al., 2014; Prescher et al., 2015) indicate that it can explain low V_S of the inner core without application of specific crystallization conditions (Mattesini et al., 2013; Yoshida et al., 1996) or premelting effects (Martorell et al., 2013). Indeed, Fe_3C is the next plausible compound to explain low V_S in the inner core (Gao et al., 2011; Gao et al., 2008).

The previous and present melting relationships of the Fe-Fe_3C system shown in Figure 3.5 indicate that the peritectic liquid coexisting with Fe_7C_3 shifts toward the Fe-rich side with increasing pressure. The eutectic liquid composition of the system is likely to shift toward a similar direction with increasing pressure. If Fe carbide is a liquidus phase during crystallization of the inner core, the initial crystallizing phase from the liquid core may be Fe_7C_3, followed by Fe_3C, and then by a mixture of hcp-Fe and Fe_3C at the latest stage. Crystallization of hcp-Fe and Fe_3C from the eutectic liquid provides no compositional convection in the outer core, because no light element is expelled by the crystallization. The latent heat due to crystallization will only be the energy source to create geodynamo in the outer core.

Thus, the distribution of these phases in the inner core could account for its internal structure, as revealed by seismology of the innermost inner core (Ishii & Dziewonski, 2002; Cao & Romanowicz, 2007). Our results suggest the innermost inner core of Fe_7C_3, which is consistent with a recent compression study (Nakajima et al., 2011; Chen et al., 2012). According to elasticity of Fe_7C_3 and Fe_3C determined by ab initio calculations, both carbides are highly anisotropic (Mookherjee et al., 2011; Mookherjee, 2011) and could explain anisotropy in the inner core even better than hcp-Fe. Caracas (2017), on the other hand, argued that the anisotropy of hcp-iron increases with increasing carbon content. Lai et al. (2018) showed experimentally a strong anisotropy of Fe_7C_3 up to 80 GPa and 800 K, and argued that high temperature may significantly influence the elastic anisotropy. A recent seismological study (Wang et al., 2015) suggested that both the inner core and the innermost inner core have different types of seismic anisotropy. If Fe_3C and Fe_7C_3 crystallized in the core, they could cause the anisotropic structure within the inner core. We should notice

that detailed quantitative arguments on carbide layering in the inner core with its anisotropy is not possible at present due to insufficient experimental data on the phase relations of the Fe-C system under the inner core conditions and should be evaluated in future studies.

Crystallization of carbon-bearing phases would concentrate carbon in the inner core, resulting in a depletion of carbon in the outer core. Other light elements, such as H, O, Si, and S need to be present to satisfy the observed density of the outer core, since the outer core has a smaller density compared to the inner core. Although the multicomponent systems are not yet studied at high pressure to reveal liquidus phases during the inner core crystallization, carbides are very promising candidates if we compare melting temperatures of different compounds under the core conditions (FeSi by Lord et al., 2010; $Fe_{72.5}Si_{27.5}$ by Fischer et al., 2011; $Fe_{90.1}Si_{9.9}$ by Asanuma et al., 2010; $Fe_{75}O_5S_{20}$ by Terasaki et al., 2011). In the Fe-C-S system, iron carbide would be the liquidus phase, which could coexist with a sulfur-rich liquid, although the experiments are limited to 7 GPa (Dasgupta et al., 2009) and need to be confirmed at higher pressures.

ACKNOWLEDGMENTS

We thank I. Ohira, Y. Shibazaki, N. Nishitani, T. Sakairi, A. Suzuki, and M. Murakami for their technical assistance and useful discussions. We also appreciate K. D. Litasov for his advice to improve the manuscript. This work was supported by a Grant-in-Aid for Scientific Research from the Ministry of Education, Culture, Science, Sport, and Technology of Japan (Nos. 18104009, 22000002, and 15H05748) to EO. ST was supported by the Research Fellowship for Young Scientists of Japan Society for the Promotion of Science. The in-situ X-ray diffraction experiments were performed with the approval of the Japan Synchrotron Radiation Research Institute (JASRI) (Proposal Nos. 2012B1560; 2013A1496; 2013B0104; 2014A0104).

AUTHOR CONTRIBUTIONS

ST, EO, TS, IM, SK, and TS performed high-pressure experiments. ST, SO, MM, YI, KS, and NA carried out chemical analyses. NH and YO supported the in-situ XRD experiments at SPring-8. ST, EO, and TS wrote the paper. All authors discussed the results and commented on the manuscript.

REFERENCES

Akahama, Y., & Kawamura, H. (2004). High pressure Raman spectroscopy of diamond anvils to 250 GPa: Method for pressure determination in the multimegabar pressure range. *Journal of Applied Physics*, *96*, 3748–3751.

Anders, E., & Grevesse, N. (1989). Abundances of the elements: Meteoritic and solar. *Geochimica et Cosmochimica Acta*, *53*, 197–214.

Anderson, O. L., & Isaak, D. G. (2002). Another look at the core density deficit of Earth's outer core. *Physics of the Earth and Planetary Interior*, *131*, 19–27.

Anzellini, S., Dewaele, A., Mezouar, M., Loubeyre, P., & Morard, G. (2013). Melting of iron at Earth's inner core boundary based on fast X-ray diffraction. *Science*, *340*, 464–466.

Asanuma, H., Ohtani E., Sakai, T., et al. (2010). Melting of iron-silicon alloy up to the core-mantle boundary pressure: Implications to the thermal structure of the Earth's core. *Physics and Chemistry of Minerals*, *37*, 353–359.

Benz, M. G., & Elliott, J. F. (1961). The austenite solidus and revised iron-carbon diagram. *Transaction of AIME*, *221*, 323–331.

Birch, F. (1964). Density and composition of mantle and core. *Journal of Geophysical Research*, *69*, 4377–4388.

Campbell, A. J., Danielson, L., Righter, K., et al. (2009). High pressure effects on the iron–iron oxide and nickel–nickel oxide oxygen fugacity buffers. *Earth and Planetary Science Letters*, *286*, 556–564.

Campbell, A. J., Seagle, C. T., Heinz, D. L., et al. (2007). Partial melting in the iron-sulfur system at high pressure: A synchrotron X-ray diffraction study. *Physics of the Earth and Planetary Interior*, *162*, 119–128.

Cao, A., & Romanowicz, B. (2007). Test of the innermost inner core models using broadband PKIKP travel time residuals. *Geophysical Research Letters*, *34*, L08303.

Caracas, R. (2017). The influence of carbon on the seismic properties of solid iron, *Geophysical Research Letters*, *44*, 128–134. doi:10.1002/2016GL071109

Chen, B. Gao, L., Lavina, B., et al. (2012). Magneto-elastic coupling in compressed Fe_7C_3 supports carbon in Earth's inner core. *Geophysical Research Letters*, *39*, L18301.

Chen, B., Lai, X., Li, J. et al. (2018). Experimental constraints on the sound velocities of cementite Fe_3C to core pressures. *Earth and Planetary Science Letters*, *494*, 164–171.

Chen, B., Li., Z., Zhang, et al. (2014). Hidden carbon in Earth's inner core revealed by shear softening in dense Fe_7C_3. *Proceedings of the National Academy of Sciences of the United States of America*, *111*, 17755–17758.

Chi, H., Dasgupta, R., Duncan, M., & Shimizu, N. (2014). Partitioning of carbon between Fe-rich alloy melt and silicate melt in a magma ocean: Implications for the abundance and origin of volatiles in Earth, Mars, and the Moon. *Geochimica et Cosmochimica Acta*, *139*, 447–471.

Dasgupta, R., Buono, A., Whelan, G., & Walker, D. (2009). High-pressure melting relations in Fe-C-S systems: Implications for formation, evolution, and structure of metallic cores in planetary bodies. *Geochimica et Cosmochimica Acta*, *73*, 6678–6691.

Dasgupta, R., & Walker, D. (2008). Carbon solubility in core melts in a shallow magma ocean environment and distribution of carbon between the Earth's core and the mantle. *Geochimica et Cosmochimica Acta*, *72*, 4627–4641.

Dewaele A., Loubeyre, P., & Mezouar, M. (2004). Equations of state of six metals above 94 GPa. *Physical Review B*, *70*, 094112.

Dewaele, A., Loubeyre, P., Occelli, M., et al. (2006). Quasihydrostatic equation of state of iron above 2 Mbar. *Physical Review Letters*, *97*, 215504–215507.

Dubrovinsky, L. S., Saxena, S. K., Tutti, F., et al. (2000). In situ X-ray study of thermal expansion and phase transition of iron at multimegabar pressure. *Physical Review Letters*, *84*, 1720–1723.

Dziewonski, A. M., & Anderson, D. L. (1981). Preliminary reference Earth model. *Physics of the Earth and Planetary Interior*, *25*, 297–356.

Fei, Y., & Brosh, E. (2014). Experimental study and thermodynamic calculations of phase relations in the Fe-C system at high pressure. *Earth and Planetary Science Letters*, *408*, 155–162.

Fei, Y., Ricolleau, A., Frank, M., et al. (2007). Toward an internally consistent pressure scale. *Proceedings of the National Academy of Sciences of the United States of America*, *104*, 9182–9186.

Fiquet, G., Badro, J., Gregoryanz, E., Fei, Y., & Occelli, F. (2009). Sound velocity in iron carbide (Fe_3C) at high pressure: Implications for the carbon content of the Earth's inner core. *Physics of the Earth and Planetary Interiors*, *172*, 125–129.

Fischer, R. A., Campbella, A. J., Reamana, D. M., et al. (2011). Phase relations in the Fe-FeSi system at high pressures and temperatures. *Earth and Planetary Science Letters*, *373*, 54–64.

Gao, L., Chen, B., Wang, J. et al. (2008). Pressure-induced magnetic transition and sound velocities of Fe_3C: Implications for carbon in the Earth's inner core. *Geophysical Research Letters*, *35*, L17306, doi:17310.11029/12008gl034817

Gao, L., Chen, B., Zhao, J. et al. (2011). Effect of temperature on sound velocities of compressed Fe_3C, a candidate component of the Earth's inner core. *Earth and Planetary Science Letters*, *309*, 213–220.

Hirayama, Y., Fujii, T., & Kurita, K. (1993). The melting relation of the system, iron and carbon at high pressure and its bearing on the early stage of the Earth. *Geophysical Research Letters*, *20*, 2095–2098.

Ishii, M., & Dziewonski, A. M. (2002). The innermost inner core of the Earth: Evidence for a change in anisotropic behavior at the radius of about 300 km. *Proceedings of the National Academy of Sciences of the United States of America*, *99*, 14026–14030.

Kamada, S., Terasaki, H., Ohtani, E., et al. (2010). Phase relationships of the Fe-FeS system in conditions up to the Earth's outer core. *Earth and Planetary Science Letters*, *294*, 94–100.

Kuwayama, Y., Hirose, K., Sata, N., & Ohishi, Y. (2011). Pressure-induced structural evolution of pyrite-type SiO_2. *Physics and Chemistry of Minerals*, *38*, 591–597.

Lai, X., Zhur, F., Liu, J. et al. (2018). The high-pressure anisotropic thermoelastic properties of a potential inner core carbon-bearing phase, Fe_7C_3, by single-crystal X-ray diffraction. *American Mineralogist*, *103*, 1568–1574. https://doi.org/10.2138/ am-2018-6527

Litasov, K. D., Sharygin, I. S., Dorogokupets, P. I., et al. (2013) Thermal equation of state and thermodynamic properties of iron carbide Fe_3C to 31 GPa and 1473 K. *Journal of Geophysical Research: Solid Earth*, *118*, 5274–5284.

Liu, J., Lin, J.-F., Prakapenka, V. B., et al. (2016). Phase relations of Fe_3C and Fe_7C_3 up to 185GPa and 5200K: Implication for the stability of iron carbide in the Earth's core. *Geophysical Research Letters*, *43*. https://doi:10.1002/2016GL071353

Lord, O. T., Walter, M. J., Dasgupta, R., et al. (2009). Melting in the Fe-C system to 70 GPa. *Earth and Planetary Science Letters*, *284*, 157–167.

Lord, O. T., Walter, M. J., Dobson, D. P., et al. (2010). The FeSi phase diagram to 150 GPa. *Journal of Geophysical Research*, *15*, B06208. https://doi:10.1029/2009JB006528.

Mao, H. K., Wu, Y., Chen, L. C., & Shu, J. F. (1990). Static compression of iron to 300 GPa and $Fe_{0.8}Ni_{0.2}$ alloy to 260 GPa: Implications for composition of the core. *Journal of Geophysical Research*, *95*, 21737–21742.

Martorell, B., Vočadlo, L., Brodholt, J., & Wood, I.G. (2013). Strong premelting effect in the elastic properties of hcp-Fe under inner-core conditions. *Science*, *342*, 466–468.

Mattesini, M., Belonoshko, A., Tkalčić, H., et al. (2013). Candy wrapper for the Earth's inner core. *Scientific Reports*, *3*, 2096. https://doi: 2010.1038/srep02096

McDonough, W. F. (2003). Compositional model for the Earth's core. In R. W. Carlson, (Ed.), *Treatise on Geochemistry 2* (pp. 547–568). Amsterdam: Elsevier.

Miyahara, M., Sakai, T., Ohtani, E., et al. (2008). Application of FIB system to ultra-high-pressure Earth science. *Journal of Mineralogical and Petrological Sciences*, *103*, 88–93.

Mookherjee, M. (2011). Elasticity and anisotropy of Fe_3C at high pressures. *American Mineralogist*, *96*, 1530–1536.

Mookherjee, M., Nakajima, Y., Steinle-Neumann, G., et al. (2011). High pressure behaviour of iron carbide (Fe_7C_3) at inner core conditions. *Journal of Geophysical Research*, *116*, B04201.

Morard, G., Andrault, D., Guignot, N., et al. (2008). In situ determination of Fe-Fe_3S phase diagram and liquid structural properties up to 65 GPa. *Earth and Planetary Science Letters*, *272*, 620–626.

Nakajima, Y., Takahashi, E., Sata, N., et al. (2011). Thermoelastic property and high-pressure stability of Fe_7C_3: Implication for iron-carbide in the Earth's core. *American Mineralogist*, *96*, 1158–1165.

Nakajima, Y., Takahashi, E., Suzuki, T., & Funakoshi, K. (2009). "Carbon in the core" revisited. *Physics of the Earth and Planetary Interior*, *174*, 202–211.Nimmo, F. (2015). Energetics of the core. In G. Schubert (Ed.), *Treatise on Geophysics* (2nd ed.). Amsterdam: Elsevier.

Ohishi, Y., Hirao, N., Sata, N., Hirose, K., & Takata, M. (2008). Highly intense monochromatic X-ray diffraction facility for high-pressure research at SPring-8. *High Pressure Research*, *28*, 163–173.

Poirier, J. P. (1994). Light elements in the earth's outer core: A critical review. *Physics of the Earth and Planetary Interior*, *85*, 319–337.

Prescher, C., Dubrovinsky, L., Bykova, E., et al. (2015). High Poisson's ratio of Earth's inner core explained by carbon alloying. *Nature Geoscience*, *8*, 220–223.

Sata, N., Hiose, K., Hirose, K., et al. (2010). Compression of FeSi, Fe_3C, $Fe_{0.95}O$, and FeS under the core pressures and implication for light element in the Earth's core. *Journal of Geophysical Research*, *115*, B09204.

Shanker, J., Singh, B. P., & Srivastava, S. K. (2004). Volume-temperature relationship for iron at 330 GPa and Earth's core density deficit. *Physics of the Earth and Planetary Interior*, *147*, 333–341.

Shen, G., Mao, H. K., & Hemley, R. J. (1996). Laser-heated diamond anvil cell technique: Double-sided heating with multimode Nd:YAG laser. In *Advanced Materials '96* (pp. 149–152) (Proc. 3rd NIRIM International Symposium on Advanced Materials).

Simon, F., & Glatzel, G. (1929). Remarks on fusion pressure curve. *Zeitschrift für anorganische und allgemeine Chemie*, *178*, 517–522.

Tateno, S. Hirose, K., Ohishi, Y., & Tatsumi, Y. (2010). The structure of iron in Earth's inner core. *Science*, *330*, 359–361.

Terasaki, H., Kamada, S., Sakai, T., et al. (2011). Liquidus and solidus temperatures of a Fe-O-S alloy up to the pressures of the outer core: Implication for the thermal structure of the Earth's core. *Earth and Planetary Science Letters*, *394*, 559–564.

Terasaki, H. Shibazaki, Y., Nishida, K. et al. (2014). Repulsive nature for hydrogen incorporation to Fe_3C up to 14 GPa. *ISIJ International*, *54*, 2637–2642.

Vočadlo, L., Brodholt, J., Dobson, D. P., et al. (2002). The effect of ferromagnetism on the equation of state of Fe_3C studied by first-principles calculations. *Earth and Planetary Science Letters*, *203*, 567–575.

Walker, D., Dasgupta, R., Li, J. & Buono, A. (2013). Nonstoichiometry and growth of some Fe carbides. *Contribution to Mineralogy and Petrology*, *166*, 935–957.

Wang, T., Song, X., & Xia, H. H. (2015). Equatorial anisotropy in the inner part of Earth's inner core from autocorrelation of earthquake coda. *Nature Geoscience*, *8*, 224–227.

Wood, B. J. (1993). Carbon in the core. *Earth and Planetary Science Letters*, *117*, 593–607.

Yoshida, S., Sumita, I.,& Kumazawa, M. (1996). Growth model of the inner core coupled with the outer core dynamics and the resulting elastic anisotropy. *Journal of Geophysical Research: Solid Earth*, *101*, 28085–28103.